Chemical Science

ROYAL SOCIETY OF CHEMISTRY

EDGE ARTICLE

View Article Online
View Journal | View Issue

Cite this: *Chem. Sci.*, 2026, **17**, 2183

All publication charges for this article have been paid for by the Royal Society of Chemistry

Tuning the anisotropic facet of Cu_2O single-crystals for photocarrier spatial segregation

Shuo Tian,[a] Yunsen Wang,[a] Shuyun Chen,[a] Zhichao Yu,[a] Di Wu,[a] Jiao Qin,[a] Dianyong Tang*[b] and Dianping Tang *[a]

Received 20th September 2025
Accepted 25th November 2025

DOI: 10.1039/d5sc07288c

rsc.li/chemical-science

Precise design of anisotropic facets is a key strategy for modulating semiconductor photoelectrochemical (PEC) performance, but it still faces significant challenges. In this work, we proposed an approach to modulate Cu_2O photoelectrodes based on triple engineering, including morphology, defect state, and crystal facet engineering, which promoted photocarrier separation through rational design of anisotropic facets. By controlling the precursors, six Cu_2O photoelectrodes with anisotropic facet structures and different oxygen vacancy (O_V) contents were obtained. The prepared Cu_2O photoelectrodes exhibited significant negative photocurrent responses to H_2O_2 catalyzed by the sandwich immunoenzyme, which enabled the development of a PEC immunoassay for the sensitive detection of carcinoembryonic antigen (CEA). The anisotropic separation of photocarriers and the highly selective recognition of target molecules could be effectively achieved by optimizing the ratio of facets exposed and the facets with characteristic adsorption. Combined with density functional theory (DFT) calculations, the electronic structure characteristics and photocarrier transfer behavior of anisotropic facets have been investigated, elucidating the critical role of crystal facet engineering in promoting the anisotropic separation of photocarriers and modulating the kinetics of surface reactions. This work provides an innovative engineering strategy for the development of PEC sensors with high photoelectric conversion efficiency.

Introduction

Photoelectrochemistry (PEC), as an emerging and rapidly developing analytical technique, has won widespread attention due to its advantages of high sensitivity, low background signal, and device miniaturization.[1–4] The photoelectric conversion efficiency is the core index that determines the performance of PEC analysis.[5,6] In addition to the energy band structure, achieving efficient photogenerated carrier separation is also the key to improving the photoelectric conversion efficiency.[7] However, photocarriers involve complex processes such as charge separation, migration, complexation, and surface reactions on time scales spanning femtoseconds to seconds, resulting in low concentrations of photocarriers arriving at the surface and kinetically retarded interfacial redox reactions.[8,9] Various strategies have been developed to improve the separation efficiency of photocarriers, including the construction of heterojunctions, co-catalyst modification, defect modulation, and crystal facet engineering.[10–14]

Crystal facet engineering is used to optimize the physicochemical properties of crystals by precisely regulating the exposure, arrangement, and surface properties of specific crystal facets.[15,16] Due to the different arrangement of atoms in different crystal facets, crystal facet engineering endows crystals with anisotropic features, which are expressed explicitly as: anisotropic surface electronic structure, anisotropic surface built-in electric field, anisotropic molecular adsorption, anisotropic photoactivity, and anisotropic photocarrier separation.[17–21] Among them, the anisotropic crystal facet could induce spontaneous polarization inside the photoelectric material, forming a built-in electric field to drive the photocarriers to achieve anisotropic segregation and migration.[22,23] For example, it was found that $SrTiO_3$ single crystals enable the effective anisotropic separation of photoexcited electron–hole pairs between {100} and {111} facets, and that the rate of photocatalytic hydrogen precipitation was much higher for anisotropic faceted $SrTiO_3$ than for isotropic faceted $SrTiO_3$.[24] Kong's group has realized the unassisted charging of zinc–air batteries by investigating anisotropic photocarrier separation on a series of representative semiconductors.[25] Although existing studies have revealed the critical role of anisotropic facets in the regulation of photoelectric properties, the mechanism by which they affect the photocarrier has not been clarified.[26] Meanwhile, realizing the precise regulation and functionalized modification of anisotropic facets remains a core challenge.

[a]*Key Laboratory for Analytical Science of Food Safety and Biology (MOE & Fujian Province), Department of Chemistry, Fuzhou University, Fuzhou 350108, P. R. China. E-mail: dianping.tang@fzu.edu.cn*

[b]*Chongqing Key Laboratory of Kinase Modulators as Innovative Medicine, College of Pharmacy (International Academy of Targeted Therapeutics and Innovation), Chongqing University of Arts and Sciences, Chongqing 402160, P. R. China. E-mail: tdy@cqwu.edu.cn*

The introduction of cutting-edge computational methods provides a revolutionary tool to solve the above challenges.[27–29] First-principles calculations based on density functional theory (DFT) enable accurate evaluation of the core properties of anisotropic facets, encompassing not only thermodynamic parameters and kinetic behaviour but also electronic structure characteristics such as band structure, electronic localization function, and surface work function.[30–32] For example, Dong's group designed and synthesized uniform all-inorganic $CsPbBr_3$ cubic/tetrahedral single-crystals with surface anisotropy. Theoretical calculations confirmed that the anisotropy difference directly affects the performance of the optoelectronic device, essentially improving light harvesting and carrier transport.[33] The close combination of experimental studies and theoretical calculations has deeply decoded the mechanism of action between anisotropic facets and photocarriers.[34] The in-depth exploration of this interdisciplinary research lays the foundation for the precise modulation of optoelectronic performance using anisotropic crystal facet engineering, leading the research towards a new level of intelligent design.

Herein, we proposed a method for crystal facet engineering to modulate semiconductor photoelectrodes, which promoted the spatial separation of photocarriers by rationally designing the anisotropic facets of Cu_2O single-crystals (Scheme 1). Six anisotropic Cu_2O photoelectrodes with tunable structural symmetry and precisely controlled exposed {100}/{111} facets were successfully synthesized by tuning the ratio of precursors and morphological tailoring. It is shown that an appropriate exposure ratio of {100} and {111} facets could effectively promote the separation and migration of photocarriers on the anisotropic facets, thus significantly enhancing the sensing performance. The prepared Cu_2O photoelectrodes exhibited significant negative photocurrent responses to H_2O_2 catalysed by the sandwich immunoenzyme, which enabled the development of a PEC immunosensor for sensitive detection of carcinoembryonic antigen (CEA). The electronic structure characteristics of the anisotropic surface and the surface reaction mechanism were described by combining experimental validation with DFT calculations. In this study, the mechanism of anisotropic facets regulating the anisotropic separation of photocarriers was essentially elucidated by modelling the regulation of atomic configuration–electronic structure–carrier separation on the surface. It not only provides a new perspective for optimizing the photoelectric conversion efficiency through crystal facet engineering, but also lays down the theoretical support and design basis for the development of highly sensitive and anti-interference PEC sensors.

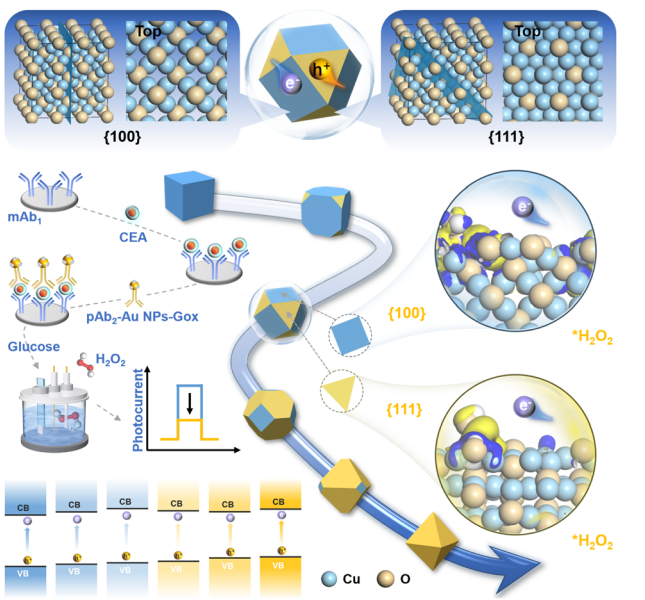

Scheme 1 Schematic illustration of tuning the anisotropic facet of Cu_2O single-crystals for photocarrier spatial segregation-based photoelectrochemical immunoassay.

Results and discussion

Characterization of x-Cu_2O

By introducing the surfactant polyvinylpyrrolidone (PVP), six anisotropic Cu_2O photoelectrodes with tunable structural symmetry and precisely controlled exposed {100}/{111} facets were successfully prepared. Regulating PVP concentration enabled precise control over the exposure ratio of specific crystal facets.[35] The regulatory mechanism of PVP concentration on anisotropic crystal facet exposure was thoroughly investigated. As depicted in Fig. S1, with increasing PVP dosage, the morphology of Cu_2O crystals gradually evolved from cubic (predominantly exposing the {100} facet) to octahedral (predominantly exposing the {111} facet). In the absence of PVP, the {111} facet exhibited faster growth kinetics due to its higher surface energy, forming a thermodynamically stable cubic morphology. Upon PVP introduction,

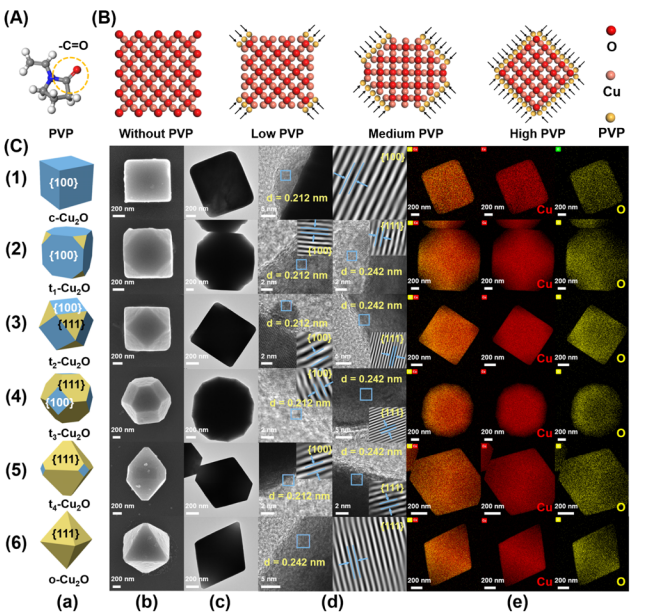

Fig. 1 (A) Chemical structure of PVP. (B) Adsorption of PVP on the crystal facets of Cu_2O. (C) (a1–a6) structural models, (b1–b6) SEM images, (c1–c6) HRTEM images, and (e1–e6) total element distribution images and single element mapping distribution of c-Cu_2O, t_{1-4}-Cu_2O, and o-Cu_2O.

the oxygen atom within the negatively charged carbonyl (C═O) group of PVP molecules could bind to Cu^+ ions exposed on the {111} facet, enhancing crystal surface stability (Fig. 1A).[36] As depicted in Fig. 1B, PVP preferentially adsorbed onto the {111} facet, enabling precise regulation of the {100}/{111} facet exposure ratio by suppressing growth kinetics on the {111} facet. With increasing PVP concentration, the proportion of {111} facet area progressively expanded until complete exposure was achieved, driving the morphology to evolve from cubic to asymptotically truncated polyhedral and octahedra (Fig. S2). During the post-synthesis treatment process, the desorption of PVP led to the exposure of unsaturated Cu coordination sites on the Cu_2O surface, commonly referred to as oxygen vacancies (O_{Vs}). As PVP concentration variations modulated differences in atomic arrangement across crystal facets, the O_{Vs} concentration also exhibited an evolution corresponding to the crystal facet changes.

Fig. 1C(a1–a6) and S3–S8 show the structural models and unfolded diagrams of six different morphologies of Cu_2O crystals, respectively. Cubic Cu_2O (c-Cu_2O) consisted entirely of the {100} facets, octahedral Cu_2O (o-Cu_2O) consisted entirely of the {111} facets, and truncated-polyhedron Cu_2O (t_{1-4}-Cu_2O) consisted of the {100} facets and the {111} facets, which were exposed at different ratios. The morphologies and microstructures of c-Cu_2O, t_{1-4}-Cu_2O, and o-Cu_2O were observed by scanning electron microscopy (SEM) (Fig. 1C(b1–b6)) and high-resolution transmission electron microscopy (HRTEM) (Fig. 1C(c1–c6)). The multi-particle TEM images are shown in Fig. S9. Unsurprisingly, the synthesized c-Cu_2O, t-Cu_2O, and o-Cu_2O nanostructures exhibited cubic, asymptotically truncated polyhedral, and octahedral morphological features, respectively. As shown in Fig. 1C(d1–d6), the lattice stripes were clear and well-defined, matching the crystals. The lattice spacing was 0.212 nm, which corresponds to the {100} facet of Cu_2O. The lattice spacing was 0.242 nm, which corresponds to the {111} facet of Cu_2O. Elemental mapping confirms that Cu and O elements were uniformly distributed in all crystals (Fig. 1C(e1–e6)).

The crystal structures of c-Cu_2O, t_{1-4}-Cu_2O, and o-Cu_2O were determined using X-ray diffraction (XRD). As demonstrated in Fig. 2A, all six products were pure, single-phase Cu_2O, with characteristic diffraction peaks matching the standard JCPDS card (No. 78-2076). It should be noted that the absence of the {100} diffraction peak in the XRD pattern of Cu_2O crystals was due to systematic absence caused by the symmetry of its crystal structure.[37] The {100} facet ($h = 1$, $k = 0$, $l = 0$) violated both the parity rule (mixed odd/even indices) and the sum rule ($h + k + l =$ odd), leading to systematic absence. In addition, the {111} diffraction peak intensity of o-Cu_2O was higher than that of c-Cu_2O and t_{1-4}-Cu_2O. The relative intensity of diffraction peaks in the samples, as calculated, is shown in Fig. 2B.

The elemental compositions and chemical states of c-Cu_2O, t_{1-4}-Cu_2O, and o-Cu_2O were analysed using X-ray photoelectron spectroscopy (XPS). The survey spectra showed the presence of Cu, O, and C elements (Fig. 2C). In the Cu 2p spectra, two peaks located at 932.5 and 952.5 eV were attributed to Cu $2p_{3/2}$ and Cu $2p_{1/2}$, respectively, which confirmed the presence of the Cu element in Cu_2O in the Cu^+ dominant state (Fig. 2D). In the O 1s spectra, the two peaks located at 530.45 and 532.37 eV were attributed to lattice oxygen (O_L) and O_{Vs}, respectively. The formation of O_{Vs} was attributed to the unsaturated coordination of Cu on the Cu_2O surface, arising from the adsorption of Cu

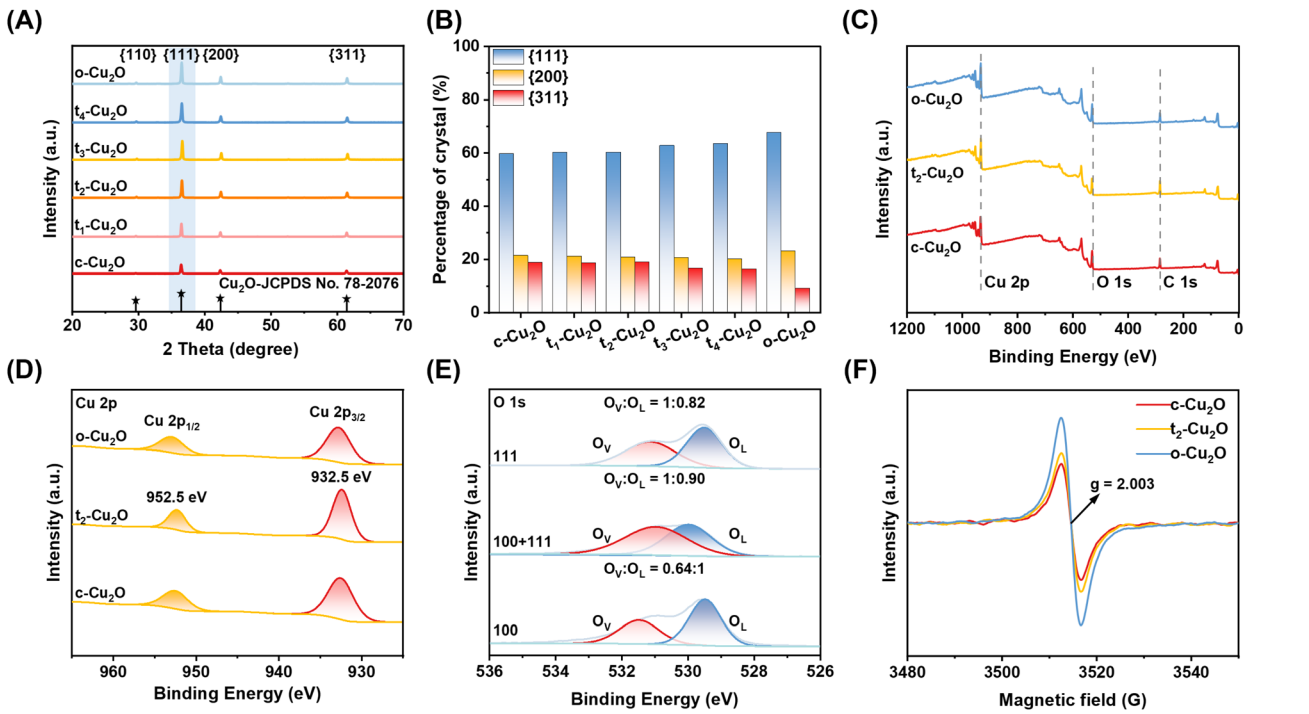

Fig. 2 (A) XRD pattern. (B) Columnar distribution of relative intensities of statistical characteristic diffraction peaks. (C) XPS survey spectra, high-resolution XPS spectra of (D) Cu 2p and (E) O 1s. (F) EPR spectra of c-Cu_2O, t_{1-4}-Cu_2O, and o-Cu_2O.

atoms onto PVP during Cu_2O crystal growth.[38] The introduction of PVP impeded {100} facet growth and displaced surface oxygen termination groups. The presence of O_{Vs} confirmed the successful removal of PVP adsorbed onto the Cu_2O surface. Among them, the peak areas of the O_{Vs} showed a significant positive correlation with the exposed area of the {111} facets in Cu_2O (Fig. 2E).

The shift in the O 1s binding energy originated from the facet-dependent surface electronic structure reconstruction. The difference in coordination environments between the {111} and {100} facets led to changes in the surface electronic states.

The electron paramagnetic resonance (EPR) technique provided a key means of elucidating the distribution of defect states in semiconductor materials, allowing precise resolution of the electronic structure of O_{Vs} and interstitial defects.[39] The presence and relative content of O_{Vs} on the Cu_2O surface were verified using EPR. As shown in Fig. 2F, the c-Cu_2O, t_{1-4}-Cu_2O, and o-Cu_2O samples all exhibited significant signal responses around a g value of 2.003, corresponding to free electrons trapped by surface O_{Vs}. In addition, the peak intensity of the O_{Vs} was positively correlated with the exposed area of the {111} facets. Precise tuning of the exposure ratio of the crystal facet could achieve the targeted optimization of the vacancy density in Cu_2O and enhance the photoelectric conversion performance of the photoelectrodes. The successful synthesis of anisotropic Cu_2O single-crystals was confirmed by the above test methods.

Characterization of photoelectric conversion efficiency

To investigate the role of crystal facet engineering in modulating the photoelectric conversion efficiency of Cu_2O, transient photocurrent testing of the photoelectrodes was performed. As shown in Fig. 3A, the t_2-Cu_2O photoelectrode with highly continuous anisotropic crystal facets exhibited the most excellent photocurrent response. This is because the anisotropic facets of the crystals could effectively promote the spatial separation of photocarriers, which significantly enhanced the photoelectric conversion efficiency of the material. To validate the effectiveness of the detection strategy and advance the construction of the PEC immunosensing platform. Six photoelectrodes were tested for feasibility and their interactions with H_2O_2 were investigated. The photocurrent response of the t_2-Cu_2O photoelectrode was found to be significantly reduced. In contrast, the other photoelectrodes did not respond significantly to H_2O_2 catalytically produced by sandwich immune enzyme catalysis with a slight decrease in photocurrent signal intensity, which could be attributed to the selective difference of the anisotropic facets in recognizing the target molecules.

To further investigate the anisotropic facet optical properties and electronic structure of the photoelectrodes, characterization was performed using ultraviolet-visible diffuse reflectance spectroscopy (UV-Vis DRS) and valence band X-ray photoelectron spectroscopy (XPS-VB). UV-Vis DRS was performed using a spectrophotometer equipped with an integrating sphere accessory, with the absorption characteristics derived from reflectance *via* the Kubelka–Munk function (Fig. S10 and 11). As illustrated in Fig. 3B, all samples exhibited a broad absorption range spanning from 200 nm to 570 nm. The contribution of monochromatic photon energy to photocurrent density was evaluated by IPCE with the following formula:[40,41]

$$\mathrm{IPCE} = \frac{1240 \times J_{\mathrm{ph}}}{\lambda \times P_{\lambda\text{-in}}} \quad (1)$$

where J_{ph} is the photocurrent density at −0.20 V *versus* Ag/AgCl, λ is the wavelength of Xe-lamp monochromatic light, and $P_{\lambda\text{-in}}$ represents incident optical power density (Table S1). As shown in Fig. 3C, the IPCE value peaks at approximately 400 nm and decreases significantly towards the visible region. Among these, the t_2-Cu_2O photoelectrode with a highly continuous anisotropic surface exhibited the highest IPCE value across the entire tested wavelength range, confirming the enhancing effect of the anisotropic facet on the photoelectric conversion efficiency within the 400–550 nm wavelength range. To verify whether the enhanced photocurrent originated from improved light absorption, absorbed photon-to-current efficiency (APCE) was evaluated using the following equation:[42]

$$\mathrm{APCE} = \frac{\mathrm{IPCE}}{\eta_{\mathrm{abs.}}(\lambda)} \quad (2)$$

$$\eta_{\mathrm{abs.}} = (1 - 10^{-A})$$

where $\eta_{abs.}$ is the light absorption efficiency, and A represents the absorbance. As depicted in Fig. 3D, the sustained enhancement of APCE for the t_2-Cu_2O photoelectrode across 400–550 nm confirmed the pivotal role of efficient photocarrier separation in its photovoltaic performance. These findings demonstrated that optimizing photocarrier separation kinetics through anisotropic crystal facet modulation substantially elevated photoelectric conversion efficiency. Compared with other studies (Table S2), photoelectrodes engineered with anisotropic facets exhibited superior PEC performance.

The forbidden bandwidth (E_g) of the photoelectrodes was determined using a Tauc plot based on the following equation:

$$(\alpha h\nu)^{1/n} = A(h\nu - E_{\mathrm{g}})$$

where α, h, ν, and A represent the absorption coefficient, Planck's constant, frequency, and constant, respectively. Considering that Cu_2O is a direct bandgap semiconductor, n takes the value of 0.5, and the E_g of Cu_2O is about 1.90 eV (Fig. 3E). The XPS-VB spectrum reflects the position of the valence band (VB) relative to the Fermi level (E_F).[43] As shown in Fig. 3F, extending the straight portion near 0 eV intersected the horizontal extension line, and the x-coordinate at this intersection point indicated the VB position. The relative position of the E_F was determined *via* electrochemical measurement of the Mott–Schottky (MS) plot (Fig. 3G), thereby establishing the position of the VB.[44] Subsequently, the position of the conduction band (CB) was calculated using the formula $E_{CB} = E_{VB} - E_g$.

Possible sensing mechanism

Combined with these results, the energy band structure of Cu_2O, as well as the potential PEC immunoreaction mechanism, was

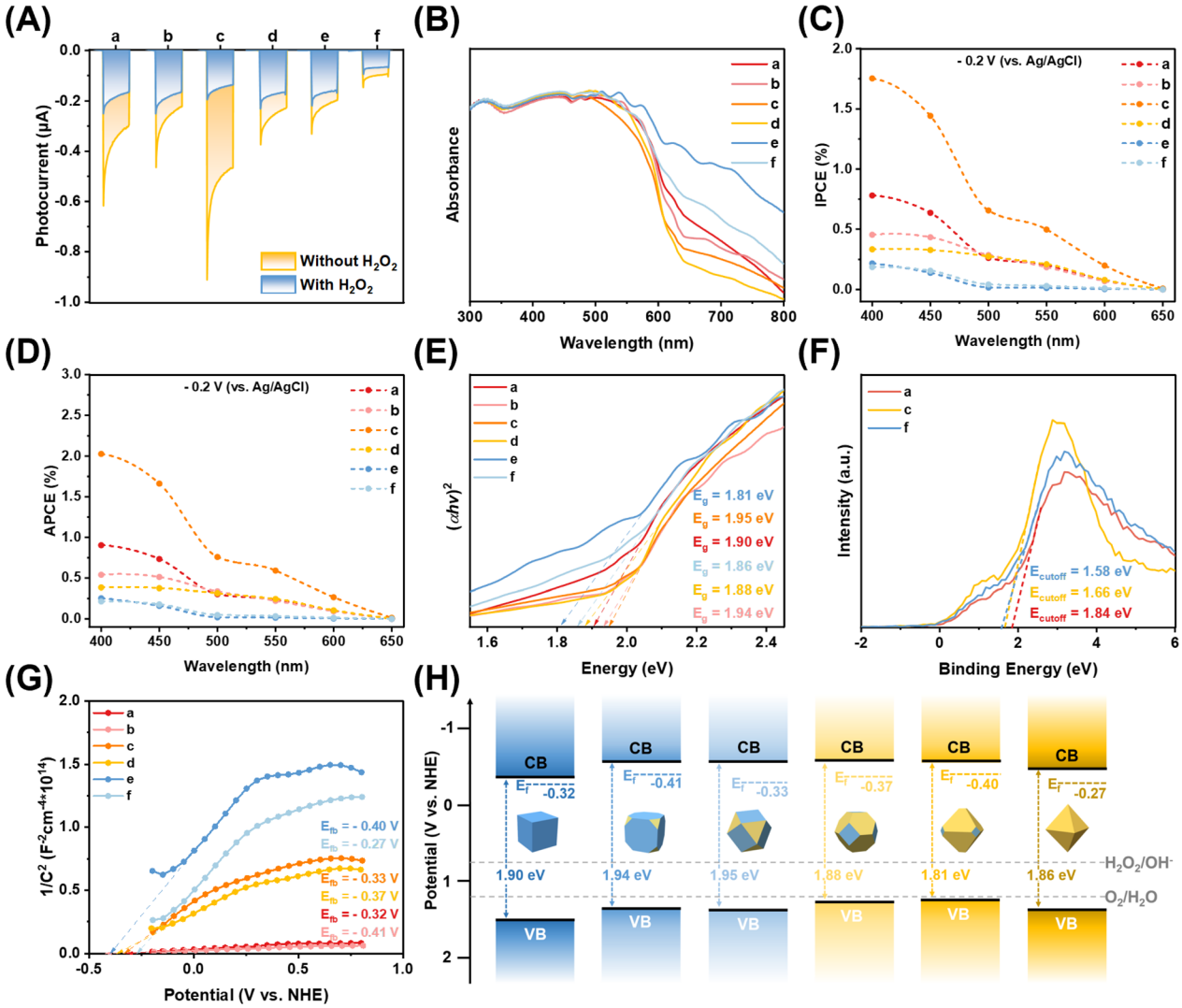

Fig. 3 (A) Photoelectric response curves, (B) UV-vis diffuse reflectance spectra, (C) IPCE plot, (D) APCE plot, (E) bandgap width spectra, (F) XPS-VB spectra, and (G) Mott–Schottky plot of (a) c-Cu_2O, (b) t_1-Cu_2O, (c) t_2-Cu_2O, (d) t_3-Cu_2O, (e) t_4-Cu_2O, and (f) o-Cu_2O. (H) Possible sensing mechanism.

determined (Fig. 3H). At the initial stage, dissolved oxygen in solution captures electrons in the CB through a $4e^-$ transfer process, generating a cathodic photocurrent. When the CEA was present, a typical sandwich-type immunoreaction was performed on a 96-well microtiter plate, where polyclonal secondary antibodies coupled to gold nanoparticles labeled with glucose oxidase (GOx–Au NPs–pAb_2) and a monoclonal CEA capture antibody (mAb_1) react with the target, and glucose oxidase (GOx) catalyses the cleavage of glucose from the substrate to produce H_2O_2. As the H_2O_2 concentration increases, the reaction pathway shifts, from the initial $4e^-$ process to $2e^-$ process, with a significant decrease in the rate of electron consumption. This transition led to an increase in the photocarrier complex efficiency, which in turn triggers the attenuation of the photocurrent signal.

Anisotropy of photocarrier separation

The electron transfer mechanism of the anisotropic facets of Cu_2O during the PEC process was revealed by density-functional theory (DFT) calculations. First, the Cu_2O bulk structure was optimized (Fig. S12), according to which the cleavage facets of {100} and {111} facets were constructed (Fig. 4A). The construction of the molecular adsorption model was continued and the anisotropic crystal surface was optimized (Fig. S13). To shed light on the reason why anisotropic crystal facets promoted photocarrier separation, the electronic energy band structures and density of state (DOS) distributions of the {100} and {111} crystal facets of Cu_2O were compared (Fig. 4B–E). Although the theoretically calculated bandgap values are usually lower than the experimentally measured values, it was feasible to calculate relative bandgap values using a consistent exchange–correlation function.[45] It was confirmed that there was a significant band energy level difference between {100} and {111} facets. The electron localization function (ELF) could measure the degree of localization of electrons in space, with values ranging from 0 to 1. A value of 1 indicates that the electron is completely localized, while a value of 0 indicates that the electron is completely delocalized. It was found that the

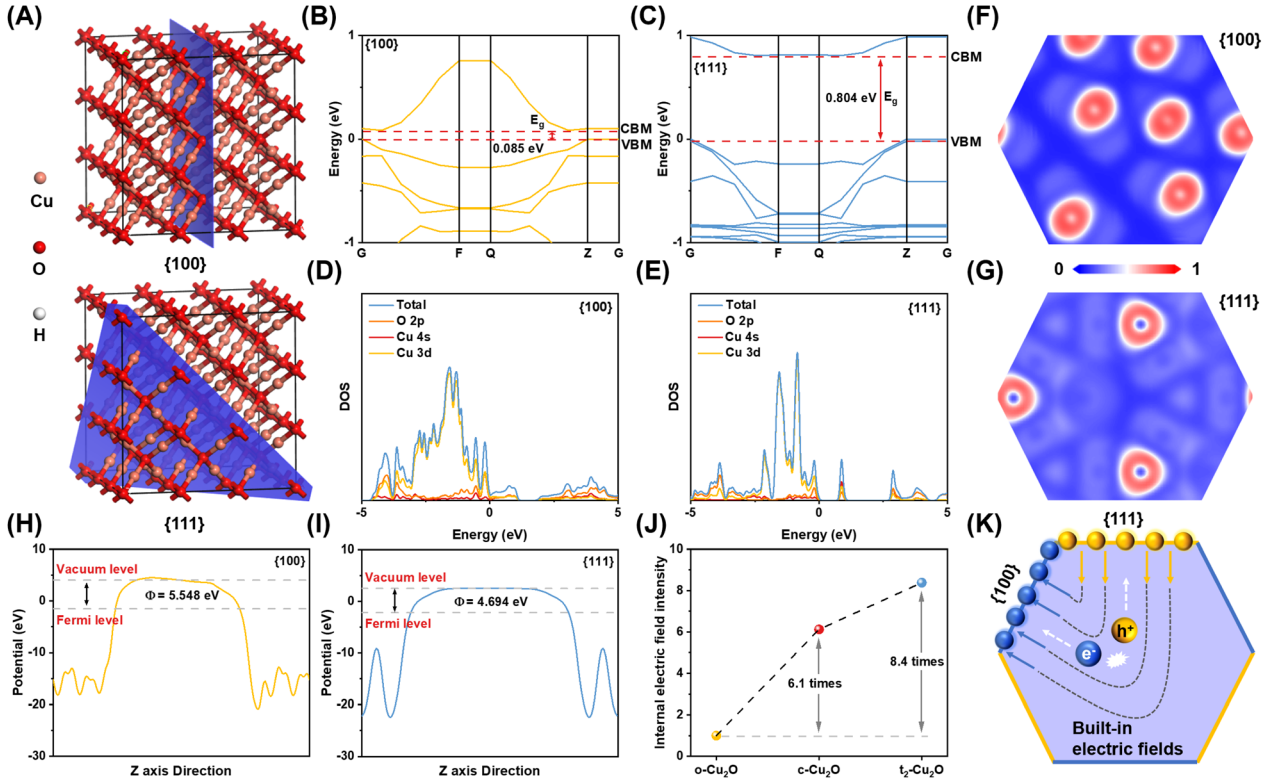

Fig. 4 Photocarrier anisotropic separation among {100} and {111} facets. (A) Crystal facet models of {100} and {111} facets. Electronic band structures of (B) {100} and (C) {111} facets (CBM: Conduction Band Minimum; VBM: Valance Band Maximum). Density of states of (D) {100} and (E) {111} facets (the Fermi level is set to 0 eV). Electron localization function of (F) {100} and (G) {111} facets. Work functions of (H) {100} and (I) {111} facets. (J) Internal electric field intensity of o-Cu_2O, c-Cu_2O, and t_2-Cu_2O (assuming the intensity of o-Cu_2O to be "1"). (K) Schematic illustration of photocarrier separation driven by built-in electric fields at the cross-section of the Cu_2O crystal.

{100} facet showed a higher degree of electron localization, while the {111} facet exhibited a higher electron delocalization feature. The higher the degree of electron delocalization, the weaker the electron was bound and the stronger the ability to polarize its motion. Therefore, electrons were more easily spilled from the {111} facet (Fig. 4F andG). The work function (Φ) could be used as a basis for judging the direction of the built-in electric field formed between the crystal facets, and the electrons tended to migrate from the surface with a lower Φ to the surface with a higher Φ.[46] Therefore, electrons on the {111} facet (Φ = 4.694 eV) would migrate to the {100} facet (Φ = 5.548 eV) until the Fermi energy levels equilibrate, forming a stable built-in electric field in the {111}–{100} direction (Fig. 4H and I). The built-in electric field reflected the strength of the charge separation drive, which was assessed by surface voltage and surface charge density studies (Fig. S14–16).[47,48] The computational results showed that t_2-Cu_2O exhibits the strong built-in electric field compared with o-Cu_2O and c-Cu_2O, which provided a strong driving force to realize effective charge separation and migration between anisotropic crystal facets (Fig. 4J). This indicated that the photogenerated electrons and holes tended to migrate toward the {100} and {111} facets, respectively, driven by the built-in electric field (Fig. 4K).

Anisotropy of molecular adsorption

During the PEC reaction, molecules in solution were adsorbed on the semiconductor surface for redox reactions with photogenerated electrons or holes. Therefore, the effective adsorption of molecules was the key link for the PEC reaction to be carried out smoothly. The adsorption of molecules on different crystal facets varies due to the various arrangements of surface atoms on different crystal facets.[49] Theoretical calculations enabled an in-depth investigation of the interactions between molecules and semiconductor surfaces. Fig. 5A presents the most stable structure formed by the anisotropic facets upon the adsorption of O_2 and H_2O_2. The difference in adsorption energies of H_2O_2 and O_2 on the {100} and {111} crystal facets of Cu_2O was further compared (Fig. 5B). The results showed that both molecules could be spontaneously adsorbed on the surface. Among them, O_2 adsorbed more strongly on the {111} facets, while H_2O_2 showed stronger adsorption capacity on the {100} facets. It was inferred that the {100} surface could adsorb and activate H_2O_2 more efficiently than the {111} surface during the PEC process, which in turn created favourable conditions for the subsequent redox reactions to proceed smoothly.

The charge distribution characteristics of the stable adsorption configurations were analysed by the charge density difference method. As shown in Fig. 5C, the molecular adsorption and charge inflow (outflow) behaviours on the {100} and {111} facets are depicted, respectively. Specifically, the yellow region (electron depletion region) was distributed on the surface of Cu–O active sites. In contrast, the blue region (electron accumulation region)

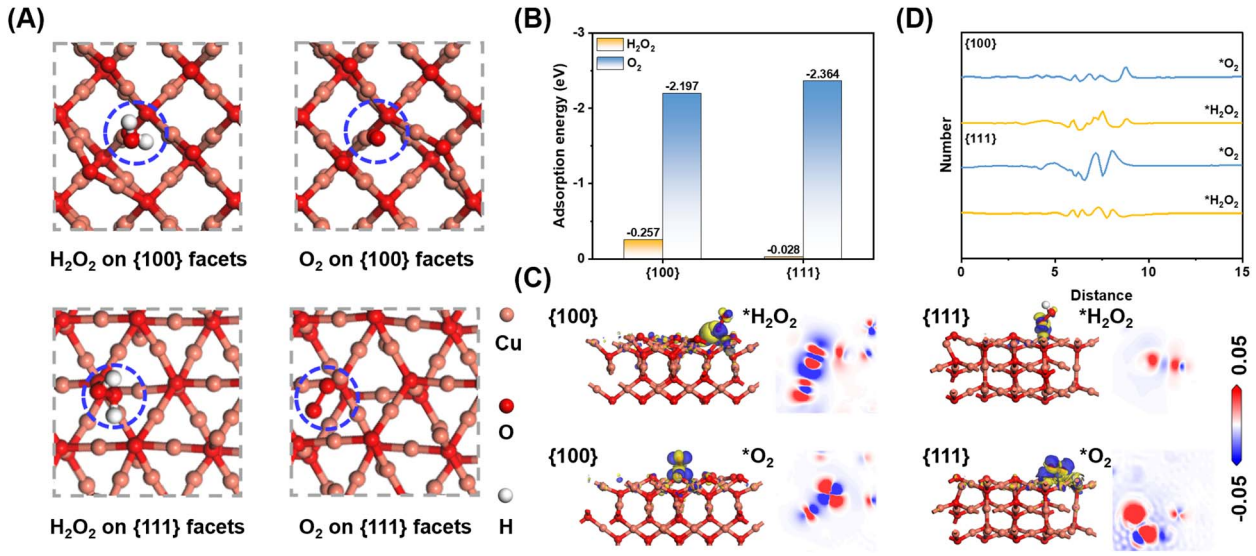

Fig. 5 (A) Optimized adsorption models for different adsorbates on the {100} and {111} facets of Cu_2O. (B) Adsorption energy diagram of different adsorbates on {100} and {111} facets. (C) Differential charge density analysis of different adsorbates on {100} and {111} adsorption models. (D) The variation of electron transfer number along the *c*-axis of the cell as a function of distance.

was concentrated on the adsorbed molecules. This phenomenon suggested that O_2 and H_2O_2 acted as electron acceptors in the reaction, and electrons flowed from the material surface to the adsorbed molecules, which in turn drove carrier transport. The molecular adsorption properties on anisotropic facets were determined by combining differential images at specific angles. A more detailed analysis of the interfacial electron transfer behaviour along the *c*-axis direction in Fig. 5D revealed a significant change in the electron transfer at the molecule–surface junction. Specifically, there was a slight difference in charge transfer between O_2 and H_2O_2 on the {100} facet, whereas there was a significant difference in charge transfer on the {111} facet, which tended to adsorb O_2 more. This change plausibly explained the more favourable adsorption behaviour of H_2O_2 on the {100} facet, confirming the key role of the anisotropic charge transfer mechanism in modulating the reaction pathway.

Photocarrier spatial segregation-based immunoassay

Based on the above discussion, in this study, we constructed a PEC biosensor using t_2-Cu_2O as a photoelectrode material to enable sensitive detection of CEA. Quantitative analysis of the target antigen CEA was performed using the developed PEC biosensor under optimal experimental conditions. As shown in Fig. 6A, the photocurrent response showed a gradual decay with the gradual increase of CEA concentration. The photocurrent signals recorded by the PEC biosensor showed a desirable linear relationship with the CEA concentration in the logarithmic interval of 0.01–50 ng mL^{-1}. The linear regression equation was $I\,(\mu A) = 0.1959 \log C_{CEA} - 0.4554$ (ng mL^{-1}, $R^2 = 0.9960$, $n = 9$) (Fig. 6B), and the limit of detection (LOD) for CEA was calculated as 9.310 pg mL^{-1} (S/N = 3). In the presence of low target concentrations, efficient photocarrier separation dominated by anisotropic crystal facets enabled rapid charge migration at the interface, yielding pronounced photocurrent spikes. At high target concentrations, redox reactions of the target substance dominated charge transfer dynamics, resulting in significantly attenuated spikes. Compared with other existing methods (Table S3), the PEC biosensor developed showed significant advantages in both the detection range and sensitivity.

Stability and specificity serve as critical metrics of sensor performance.[50] The photocurrent response exhibited high stability during 10 continuous light-on/off cycles in the presence of 10 ng per mL CEA, with a relative standard deviation (RSD) of 2.45% (Fig. 6C). Given the susceptibility of Cu_2O to photocorrosion, the long-term stability of the PEC biosensor under illumination conditions was further evaluated. As shown in Fig. S17 and 18, the Cu_2O photoelectrode demonstrated excellent cycling stability during 12 000 seconds light-on/off cycles and maintained stability over a 10-day duration. Additionally, parallel testing of five photoelectrodes incubated with 50 ng mL^{-1} of CEA resulted in a RSD of 3.14%. The results indicated that the sensor exhibited satisfactory reproducibility (Fig. 6D).

To assess the selectivity of the sensor, other common interfering substances in serum samples, including alpha-fetoprotein (AFP), prostate-specific antigen (PSA), and human epidermal growth factor receptor 2 (HER2), were selected to carry out interference experiments. As shown in Fig. 6E, the photocurrent response generated by the sensor to the target CEA was significantly reduced regardless of whether the target CEA was present alone or coexisted with the interfering substance, confirming exceptional selectivity.

To evaluate the practical performance of the PEC biosensor in the detection of real samples, the same serum samples were tested and compared with a commercially available CEA enzyme-linked immunosorbent assay (ELISA) kit. The results showed that the t_{exp} of all samples was less than 2.78 ($t_{crit[0.05,\,4]} = 2.78$) (Table S4), indicating no significant difference between the two assays for the detection of CEA. These findings collectively validated the

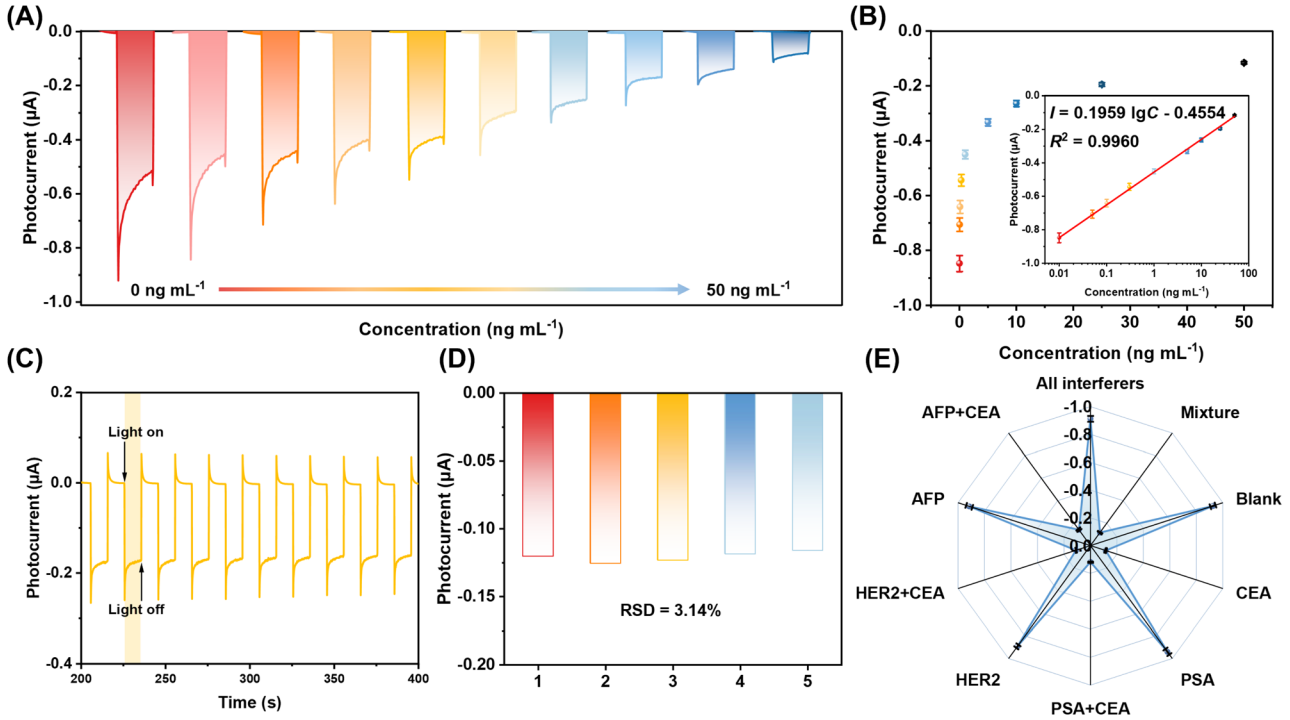

Fig. 6 (A) Monitoring photocurrent intensities of gradient concentrations (0, 0.01, 0.05, 0.1, 0.3, 1, 5, 10, 25, and 50 ng mL^{-1} CEA) based on the PEC biosensor. (B) Photocurrents of the developed PEC biosensors towards CEA standards with various concentrations (inset: Linear relationship between photocurrent intensity and the logarithm of CEA concentration). (C) Stability of the PEC biosensor in the absence and presence of 10 ng mL^{-1} CEA. (D) Reproducibility of the PEC biosensor after responding to CEA (50 ng mL^{-1}). (E) Corresponding selectivity of the constructed PEC biosensor for 50 ng mL^{-1} CEA by comparing with interfering proteins added at the 5 μg mL^{-1} level.

high accuracy and stability of the developed PEC biosensor, highlighting its substantial potential for applications in early cancer screening and health monitoring. The above findings confirmed that the constructed PEC biosensor had high accuracy and stability, and it showed a broad application prospect in the field of early cancer screening and health monitoring.

Conclusions

In conclusion, we developed a triple engineering strategy for Cu_2O photoelectrodes, which precisely controlled the anisotropy of {100} and {111} facets by modulating the morphology structure and the ratio of exposed crystal facets, and significantly improved the PEC sensing performance. The prepared t_2-Cu_2O exhibited excellent sensing properties, including high response and selectivity, and exhibited a significant negative photocurrent response to H_2O_2 catalytically generated by the sandwich immunoenzyme, and the PEC immunosensor was successfully constructed for the sensitive detection of CEA. The energy level difference between the {100} and {111} facets was utilized to form a built-in electric field, which effectively drove the anisotropic separation and migration of photocarriers. Combining experimental and theoretical calculations, the contribution of the anisotropic facets to modulating the photocarrier transfer behaviour and surface photochemical reactions was verified. This study demonstrates the critical roles of morphological tailoring and anisotropic crystal facet engineering in optimizing the PEC performance of semiconductors. It provides theoretical guidance and experimental basis for a deeper understanding of the efficient separation mechanism of photocarriers.

Experimental

Synthesis of x-Cu_2O

The synthesis of x-Cu_2O was carried out based on published literature, and the preparation procedure was described in detail.[51] First, *X* g of PVP and 90 mL of deionized water were added to a beaker. Then, 10 mL of $CuCl_2 \cdot 2H_2O$ solution (0.1 M) was added to the beaker, followed by the gradual addition of 10 mL of NaOH solution (2 M). After stirring for 30 min, 10 mL of ascorbic acid solution (0.6 M) was added gradually and stirred for 3 h. The reaction was continuously stirred at 55 °C throughout. Subsequently the product was then centrifuged and washed three times with ionised water and three times with ethanol. The product was dried at 60 °C for 5 h and the powder was collected. Finally, the x-Cu_2O powder was heated to 200 °C in a tube furnace to remove the PVP from the surface at a temperature increase rate of 5 °C min^{-1}. The protective gas was a mixture of propylene (8%), oxygen (4%) and nitrogen (88%). The reducing/oxidising gas mixture effectively oxidises the PVP on the surface of Cu_2O while preventing the oxidation of Cu_2O. Depending on the amount of PVP added, six different samples were obtained, namely c-Cu_2O (0 g PVP), t_1-Cu_2O (0.741 g PVP), t_2-Cu_2O (1.481 g PVP), t_3-Cu_2O (2.222 g PVP), t_4-Cu_2O (3.704 g PVP), and o-Cu_2O (4.444 g PVP).

Immunoassay procedure

In this paper, t_2-Cu_2O was used as the photoelectrode material, and combined with a sandwich immunoassay to catalyse glucose to produce H_2O_2 for achieving CEA detection. The analytical platform consisted of t_2-Cu_2O-modified fluorine-doped tin oxide (FTO) electrodes, mAb_1-coated microplates, glucose oxidase and detection antibody-conjugated AuNPs (GOx–Au NPs–pAb_2) (SI). In the pre-prepared mAb_1-coated microtiter plates described above, standard concentrations of analytes or treated real samples were added and incubated at 37 °C for 30 min. GOx–Au NPs–pAb_2 (50 μL, 1.0 mg mL^{-1}) was introduced into the above to promote the formation of a sandwich immune complex. The microtiter plate was then washed with PBS buffer solution (pH 7.4) to remove incompletely bound non-specific complexes, followed by the addition of 5.0 mM glucose solution (50 μL) to initiate the target catalytic reaction, and incubated for an additional 30 min at 37 °C. As the catalytic reaction proceeded, the substrate glucose was continuously catalysed to generate H_2O_2. Finally, the product H_2O_2 was introduced into Na_2SO_4 solution (0.1 M) and mixed thoroughly. The photocurrent response was measured at 0 V potential using t_2-Cu_2O as the working electrode and a 500 W xenon lamp as the excitation light source.

Ethical statement

All the experiments were performed according to the Guidelines of Fuzhou University (China) and approved by the ethics committee at Fuzhou University (China). Informed consent was obtained from human participants of this study.

Author contributions

Shuo Tian: conceptualization, methodology, visualization, writing, original draft preparation. Yunsen Wang: investigation, data curation, visualization, formal analysis. Shuyun Chen: data curation, visualization, formal analysis, visualization. Zhichao Yu: experimental data analysis. Di Wu: visualization, writing, original draft preparation. Jiao Qin: data curation, visualization, formal analysis. Dianyong Tang: experimental data analysis, resources, software. Dianping Tang: supervision, funding acquisition, project administration, writing – reviewing and editing.

Conflicts of interest

There are no conflicts to declare.

Data availability

The authors confirm that the data supporting the findings of this study are available within the article and/or it supplementary information (SI). Reasonable requests for additional information can be made to the corresponding authors. Supplementary information: materials and reagents, experimental characterization, calculation of built-in electric field intensity, DFT calculation, design and construction of 3d printed support devices, preparation method of Cu_2O modified fluorine-doped tin oxide, preparation of mAb_1-coated microplate, preparation of GOx/pAb_2-conjugated AuNP, monitoring of human serum samples and interlaboratory, Fig. S1–S12, and Tables S1 and S2. See DOI: https://doi.org/10.1039/d5sc07288c.

Acknowledgements

The authors acknowledge financial support from the National Natural Science Foundation of China (grant no.: 22574023, 22274022 & 21874022).

Notes and references

1 M. Sendeku, T. Shifa, F. Dajan, K. Ibrahim, B. Wu, Y. Yang, E. Moretti, A. Vomiero and F. Wang, *Adv. Mater.*, 2024, **36**, 2308101.
2 B. Shang, F. Zhao, S. Suo, Y. Gao, C. Sheehan, S. Jeon, J. Li, C. Rooney, O. Leitner, L. Xiao, H. Fan, M. Elimelech, L. Wang, G. Meyer, E. Stach, T. Mallouk, T. Lian and H. Wang, *J. Am. Chem. Soc.*, 2024, **146**, 2267.
3 F. Chen, L. Hou, Y. Gao, J. Zhou, F. Kong, D. Han and W. Zhao, *Adv. Funct. Mater.*, 2024, **34**, 2408186.
4 S. Ma, H. Lee and J. Moon, *Adv. Mater.*, 2024, **36**, 2405685.
5 Z. Wang, Y. Guo, M. Liu, X. Liu, H. Zhang, W. Jiang, P. Wang, Z. Zheng, Y. Liu, H. Cheng, Y. Dai, Z. Wang and B. Huang, *Adv. Mater.*, 2022, **34**, 2201594.
6 T. Bouwens, T. Bakker, K. Zhu, J. Hasenack, M. Dieperink, A. Brouwer, A. Huijser, S. Mathew and J. Reek, *Nat. Chem.*, 2023, **15**, 213.
7 R. Tan, Y. Qin, M. Liu, H. Wang, R. Su, R. Xiao, J. Li, L. Hu, W. Gu and C. Zhu, *Adv. Funct. Mater.*, 2023, **33**, 2305673.
8 N. Österbacka, H. Ouhbi, F. Ambrosio and J. Wiktor, *ACS Energy Lett.*, 2024, **9**, 153.
9 S. Hwang, H. Gu, J. Young, M. Steiner, A. Laursen, R. Crichton, Y. Yeh, P. Batson, L. Feldman, M. Li, K. Wyatt, A. Safari, T. Deutsch, E. Garfunkel and G. Dismukes, *ACS Energy Lett.*, 2024, **9**, 789.
10 J. Kosco, S. Gonzalez-Carrero, C. Howells, T. Fei, Y. Dong, R. Sougrat, G. Harrison, Y. Firdaus, R. Sheelamanthula, B. Purushothaman, F. Moruzzi, W. Xu, L. Zhao, A. Basu, S. De Wolf, T. Anthopoulos, J. Durrant and I. McCulloch, *Nat. Energy*, 2022, **7**, 340.
11 T. Takata, J. Jiang, Y. Sakata, M. Nakabayashi, N. Shibata, V. Nandal, K. Seki, T. Hisatomi and K. Domen, *Nature*, 2020, **581**, 411.
12 D. Hirayama, T. Kawawaki, S. Oguchi, M. Ogano, N. Kon, T. Yasuda, A. Higami and Y. Negishi, *J. Am. Chem. Soc.*, 2024, **146**, 26808.
13 F. Chen, Z. Ma, L. Ye, T. Ma, T. Zhang, Y. Zhang and H. Huang, *Adv. Mater.*, 2020, **32**, 1908350.
14 M. Li, H. Mu, R. Su, R. Liu, Y. Liu, Y. Li and F. Li, *Adv. Funct. Mater.*, 2025, **35**, 2412775.
15 M. Lee, J. Yang, H. Park, C. Moon, D. Andoshe, J. Park, C. Moon, T. Lee, K. Choi, W. Cheon, J. Kim and H. Jang, *Nano-Micro Lett.*, 2022, **14**, 48.

16 H. Rudel, M. M. Lane, C. Muhich and J. Zimmerman, *ACS Nano*, 2020, **14**, 16472.
17 S. Wang, G. Liu and L. Wang, *Chem. Rev.*, 2019, **119**, 5192.
18 C. Ma, F. Eickemeyer, S. Lee, D. Kang, S. Kwon, M. Grätzel and N. Park, *Science*, 2023, **379**, 173.
19 Y. Li, K. Luo, R. Tao, Z. Wang, D. Chen and Z. Shao, *Adv. Funct. Mater.*, 2020, **30**, 2002606.
20 S. Selcuk and A. Selloni, *Nat. Mater.*, 2016, **15**, 1107.
21 J. Zhang, K. Liu, B. Zhang, J. Zhang, M. Liu, Y. Xu, K. Shi, H. Wang, Z. Zhang, P. Zhou and G. Ma, *J. Am. Chem. Soc.*, 2024, **146**, 4068.
22 W. Jiang, C. Ni, L. Zhang, M. Shi, J. Qu, H. Zhou, C. Zhang, R. Chen, X. Wang, C. Li and R. Li, *Angew. Chem., Int. Ed.*, 2022, **61**, e202207161.
23 F. Sun, Y. Deng, J. Leng, M. Shi, C. Li, S. Jin, R. Li and W. Tian, *J. Am. Chem. Soc.*, 2024, **146**, 31106.
24 Y. Zhang, X. Wu, Z. Wang, Y. Peng, Y. Liu, S. Yang, C. Sun, X. Xu, X. Zhang, J. Kang, S. Wei, P. Liu, S. Dai and H. Yang, *J. Am. Chem. Soc.*, 2024, **146**, 6618.
25 L. Kong, Q. Ruan, J. Qiao, P. Chen, B. Yan, W. He, W. Zhang, C. Jiang, C. Lu and Z. Sun, *Adv. Mater.*, 2023, **35**, 2304669.
26 L. Jin, F. Cheng, H. Li and K. Xie, *Angew. Chem., Int. Ed.*, 2020, **59**, 8891.
27 M. Gunawan, O. Bowdler, S. Zhou, X. Fang, Q. Zhang, Y. Sakamoto, K. Sun, D. Gunawan, S. Y. Chang, R. Amal, N. Valanoor, J. Scott, J. Hart and C. Toe, *Adv. Funct. Mater.*, 2025, **35**, 2417651.
28 M. Ashraf, R. Ali, I. Khan, N. Ullah, M. Ahmad, T. Kida, S. Wooh, W. Tremel, U. Schwingenschlögl and M. Tahir, *Adv. Mater.*, 2023, **35**, 2301342.
29 R. Das, R. Paul, A. Parui, A. Shrotri, C. Atzori, K. Lomachenko, A. Singh, J. Mondal and S. Peter, *J. Am. Chem. Soc.*, 2023, **145**, 422.
30 A. Anand, A. Raj, D. Mondal, D. Maity, M. Ganesha, A. Singh, D. De and G. Khan, *Adv. Funct. Mater.*, 2025, **35**, 2417398.
31 R. Zeng, T. Liu, M. Qiu, H. Tan, Y. Gu, N. Ye, Z. Dong, L. Li, F. Lin, Q. Sun, Q. Zhang, L. Gu, M. Luo, D. Tang and S. Guo, *J. Am. Chem. Soc.*, 2024, **146**, 9721.
32 Z. Yu, Z. Xu, R. Zeng, M. Xu, H. Zheng, D. Huang, Z. Weng and D. Tang, *Angew. Chem., Int. Ed.*, 2025, **64**, e202414625.
33 S. Dong, Z. Hu, P. Wei, J. Han, Z. Wang, J. Liu, B. Su, D. Zhao and Y. Liu, *Adv. Mater.*, 2022, **34**, 2204342.
34 R. Nughays, K. Almasabi, S. Nematulloev, L. Wang, T. Bian, I. Nadinov, B. Irziqat, G. Harrison, S. Fatayer, J. Yin, O. Bakr and O. Mohammed, *Adv. Sci.*, 2024, **11**, 2404468.
35 L. Wang, R. Zhang, T. Zhou, Z. Lou, J. Deng and T. Zhang, *Sens. Actuators, B*, 2017, **239**, 211–217.
36 Y. Zhang, Z. Zhang, Y. Zhang, Y. Li and Y. Yuan, *J. Colloid Interface Sci.*, 2023, **651**, 117–127.
37 C. Folcia, J. Ortega, J. Etxebarria, L. Pan, S. Wang, C. Huang, V. Ponsinet, P. Barois and R. Pindak, *Phys. Rev. E*, 2011, **84**, 010701.
38 D. Zhang, H. Zhang, L. Guo, K. Zheng, X. Han and Z. Zhang, *J. Mater. Chem.*, 2009, **19**, 5220–5225.
39 D. Wu, Z. Yu, J. Qin, M. Li and D. Tang, *Anal. Chem.*, 2025, **97**, 10947.
40 J. Yang, T. Xu, P. Lv, Y. Su, J. Xie, Z. Li, H. Zhou and P. Chen, *Rare Met.*, 2025, **44**, 358–372.
41 F. Pan, L. Long, Z. Li, S. Yan, L. Wang, G. Lv, J. Zhang, J. Chen, G. Liang and D. Wang, *Small*, 2024, **20**, 2304846.
42 J. Zhang, L. Long, C. Zhao, G. Lv, J. Chen, W. Li, S. Yan and D. Wang, *Adv. Funct. Mater.*, 2024, **34**, 2411401.
43 L. Long, G. Lv, Q. Han, X. Wu, Y. Qian, D. Wang, Y. Zhou and Z. Zou, *J. Phys. Chem. C*, 2021, **125**, 23142–23152.
44 G. Lv, L. Long, F. Pan, J. Zhang, W. Li, P. Feng, J. Chen, Y. Zhou and D. Wang, *Small*, 2025, **21**, 2501984.
45 J. Shu, Z. Qiu, Z. Lin, G. Cai, H. Yang and D. Tang, *Anal. Chem.*, 2016, **88**, 12539.
46 Y. Zhang, Y. Li, X. Xin, Y. Wang, P. Guo, R. Wang, B. Wang, W. Huang, A. J. Sobrido and X. Li, *Nat. Energy*, 2023, **8**, 504.
47 Q. Zhang, X. Zhao, S. Gao, Y. Guo, H. Wang, Z. Liu and J. Wang, *ACS Catal.*, 2025, **15**, 6739.
48 X. Chen, J. Wang, Y. Chai, Z. Zhang and Y. Zhu, *Adv. Mater.*, 2021, **33**, 2007479.
49 S. Tian, Z. Yu, Y. Wang, S. Chen, M. Li and D. Tang, *Anal. Chem.*, 2025, **97**, 9518.
50 Y. Gao, L. Hou, F. Chen, J. Zhu, W. Zhang, W. Wang, F. Kong and Z. Zheng, *Sens. Actuators, B*, 2025, **443**, 138287.
51 X. Dai, K. Chen, M. He, K. Chen, X. Zhou, Y. Chen, C. Gong, P. Wang, P. Mao and Y. Yang, *Chem. Eng. J.*, 2024, **493**, 152515.